5 ADVANCED RESULTS

5.1 The damping term effect

As previously mentioned, the damping term is a controversial one: while it is an interesting addition to the KS equation in order to obtain stationary patterns, the physical meaning is not sufficiently clear up to this moment. The present study adopts the aforementioned time splitting finite-difference method to acquire solutions for the two-dimensional DKS equation under 3 circumstances: $\alpha = 0$, $\alpha = 0.05$, and $\alpha = 0.15$. The mesh consisted of 512×512 points with a harmonic monomodal initial pattern in the $\vec{1}_x$ direction ($\vec{q} = q_0 \vec{1}_x$), a small amplitude of 0.1, and parameters θ, K and a_μ as found in Table 4. Recapping the results from the linear stability analysis, a value of $\lambda_c = 18$ was calculated for the critical wavelength, corresponding to the maximum growth rate in the $\vec{1}_x$ direction. In this sense, each wavelength of the final pattern was estimated to be represented by 18 points.

According to the previous work of Paniconi and Elder [41], three distinct solutions in the late time limit might be expected for the DKS equation, depending on the parameter α: periodic large hexagonal morphology for higher values, an oscillatory or breathing hexagonal state for middle values, and a spatiotemporal chaotic state for lower values. However, since the present endeavor considers realistic coefficients related to the physics of sputtering, the same range of α values employed by Paniconi and Elder would not produce the same effects. Besides, in opposition to Paniconi and Elder, our study deals with an anisotropic DKS equation. Thereafter, during the first moments, linear effects lead to the selection of a well defined ripple direction; then, once nonlinear effects take over the system, cellular structures will develop (clearly seen on the $\alpha = 0.15$ case).

The undamped solution is shown in Figure 59, when $\alpha = 0$. The initial condition presented a wavenumber $q_o = 1.7181 \cdot 10^{-1}$ (14 wavelengths in the system). A disordered chaotic cellular structure is obtained for late time, with large variations of cell size and shape, as displayed in Figure 59a for $\tau = 11803$. From the L_1 curve (Figure 59b), we can see that the chaotic pattern is reached within $\tau = 500$. While a steady state isn't reached for the analyzed period, it is clear that the evolution dynamics are much slower during late time.

(a) Surface height $\bar{h}^n$ for $\tau = 11,803$
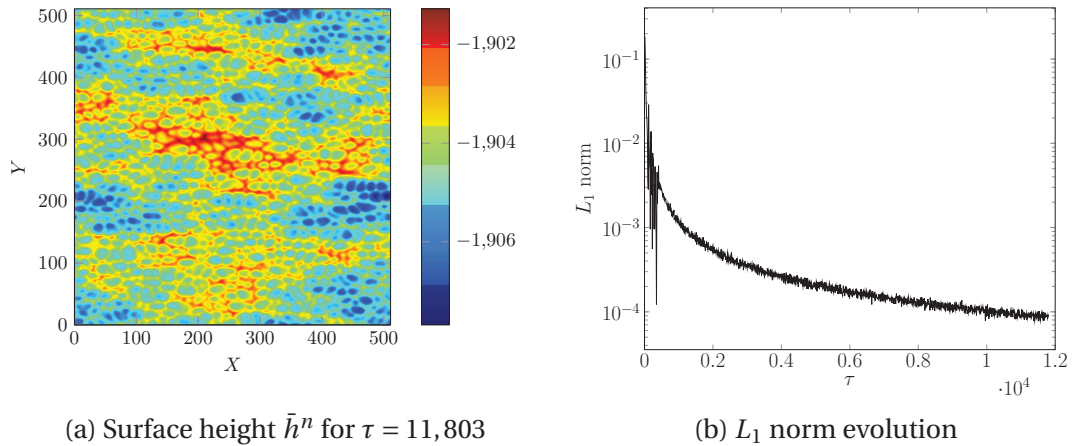
(b) L_1 norm evolution

Figure 59: Numerical solution for a 2D anisotropic DKS equation - Spatiotemporal chaotic pattern, $\alpha = 0$

Figure 60 reveals the numerical solution for $\alpha = 0.05$. The initial condition was the same from the previous case ($q_o = 1.7181 \cdot 10^{-1}$). A spatiotemporal chaotic cellular structure is obtained for late time, which can be seen in Figure 59a for $\tau = 11,750$. In comparison with the undamped structure, the late time pattern for $\alpha = 0.05$ is much more organized, with a smaller variation of cell sizes and shapes, with some of them approaching the λ_c width. The L_1 norm evolution (Figure 60b) shows that a strongly oscillatory state is reached by $\tau = 2,000$, where L_1 starts fluctuating around $L_1 = 0.02$. These intense dynamics differ from the undamped case: even though the structure is more organized, it keeps changing at a constant rate for an undefined period of time.
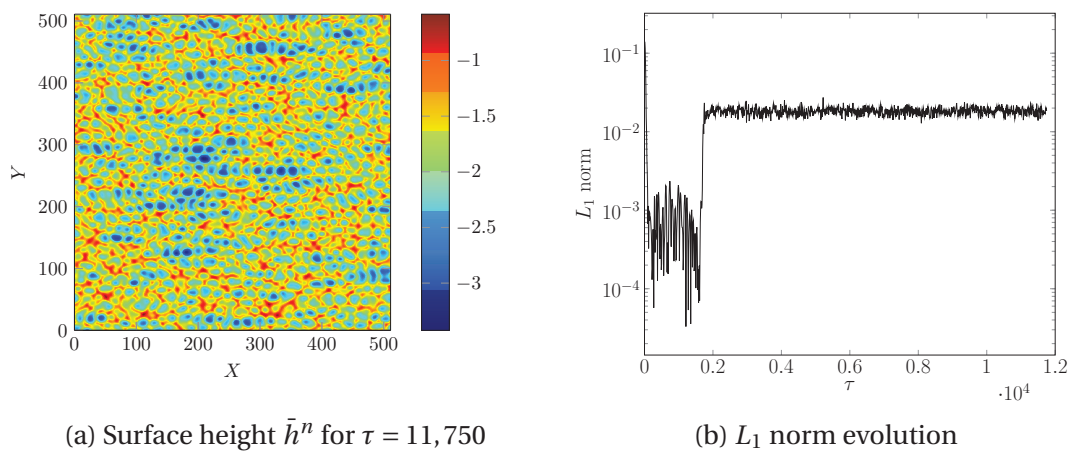

(a) Surface height $\bar{h}^n$ for $\tau = 11,750$

(b) L_1 norm evolution

Figure 60: Numerical solution for a 2D anisotropic DKS equation - Chaotic semi-organized oscillatory behavior, $\alpha = 0.05$

For higher values of α, e.g. $\alpha = 0.15$, a defect-free hexagonal structure can be obtained, as displayed by Figure 61. A smaller wavenumber $q_o = 2.4544 \cdot 10^{-2}$ was employed for the initial condition, since our previous studies revealed that an 1D structure with wavelength similar to λ_c would prevail for $q_o = 1.7181 \cdot 10^{-1}$ even in late time. Figure 61b shows that at first the L_1 norm has a continuous decline, which represents the stabilization of an 1D structure with $\vec{q} \sim \vec{q_c}$. Even though this pattern seems to be approaching a steady state, hexagonal modes emerge when τ is approaching $\tau = 2,000$, leading to a fast growth of L_1, and to the formation of a new structure. Posteriorly, L_1 reaches a peak, and the structure initiates its final stabilization, quickly removing defects and descending up to the stationary state, which is illustrated by Figure 61a for $\tau = 14,630$.

(a) Surface height $\bar{h}^n$ for $\tau = 14,630$ (b) L_1 norm evolution
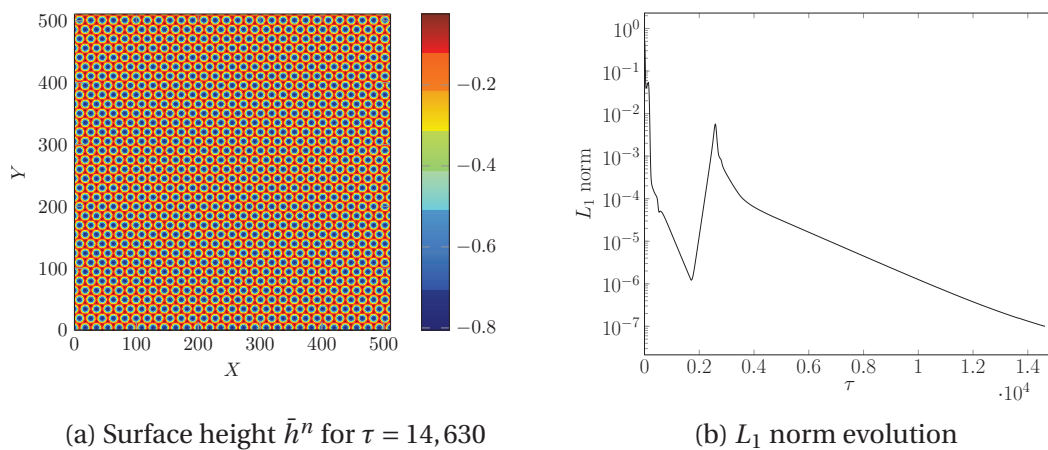
Figure 61: Numerical solution for a 2D anisotropic DKS equation - Stationary hexagonal structure, $\alpha = 0.15$

Comparing the structure evolution for $\alpha = 0.15$ and $\alpha = 0.05$, we confirm the coincident time for the emergence of the hexagonal modes, close to $\tau = 2,000$. For $\alpha = 0.15$, the damping effect is sufficient for an ordered and quick reorganization of the structure after a L_1 peak, while for $\alpha = 0.05$ the damping is not high enough to allow the nanostructure to reorganize itself into a perfectly ordered hexagonal state, and it keeps chaotically oscillating around the peak L_1 value. Another observation concerning the obtained height values must be pointed out. All of them are negative, being consistent with the erosive phenomenon. However, for $\alpha = 0$, the mean height of the surface falls continuously with time, while maintaining the distance $\bar{h}_{dif}$ between the minimum and maximum points around $\bar{h}_{dif} = 6.4$. For $\alpha = 0.05$ the mean height remains approximately constant, around -0.5 and -3.5 ($\bar{h}_{dif} \sim 3.0$), for an undefined time. Finally, for the steady state obtained with a damping $\alpha = 0.15$, the

maximum and minimum height values were, respectively, -0.03 and -0.81 ($\bar{h}_{dif} = 0.78$).

The practical significance of those results is that the acquired structures might depend on the duration of the irradiation. For a short time-duration sputtering in a system with $\alpha = 0.15$, we observe only the formation of ripples, while hexagons may emerge for a longer duration of the experiment. In contrast, for a system with $\alpha = 0$ or 0.05, the final structure will depend on time, since it keeps changing with the irradiation duration.

5.2 Anisotropy and angle of incidence

The weakly nonlinear analysis developed by Walgraef [42] investigated the parameters involved in the relative anisotropy of the resulting patterns, through the Fourier transform and adiabatic elimination. The relative anisotropy is studied by $A = \frac{\Delta}{\bar{K}q_c^4}$, where q_c is the critical wavenumber obtained from our previous linear stability analysis, and $\Delta = \frac{3}{4}(|\bar{\mu}| - |\bar{v}|)q_c^2$. Figure 62 plots the relative anisotropy A versus θ for $\bar{K} = 5$ and $a_\mu = 4$. From the plot we observe that A for $\theta = 0.5236$ (30°) is approximately 1.15, which was the value used up to this moment. The following results investigate the effect of varying the angle of incidence in the resulting pattern, motivated by this behavior of the relative anisotropy.
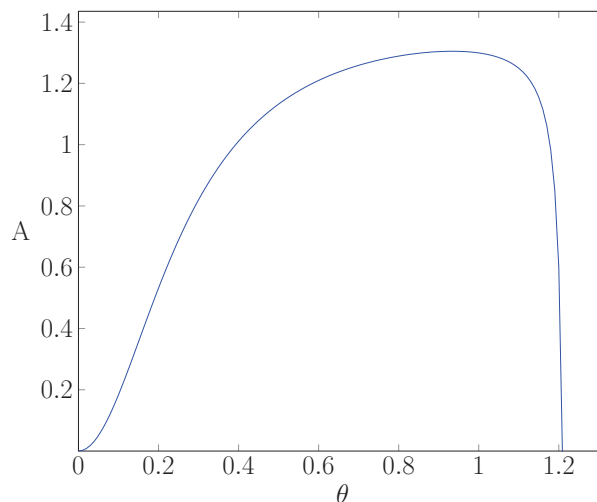

Figure 62: Relative anisotropy A versus θ for $\bar{K} = 5$ and $a_\mu = 4$

One region we are particularly interested is near $\theta = 1.2$, since v_x and v_y may present opposite signs with similar modulus. This observation implies that there will be one direction for the unstable modes where the nonlinear terms will compensate each other, as studied in the work of Rost and Krug [17]. For this simulation, we defined a θ value of 1.1549 (66.17°),

which means that we will have the following anisotropy coefficients: $v_x = 0.0658$ and $v_y = -0.0659$.

Before showing the results for our case related to the sputtering model, we would like to show a reproduction of the results from Rost and Krug. More clearly, we have introduced their same parameters in our code to compare the numerical results, which is an opportunity to present another proof of reliability for the numerical method employed in the present endeavor. The equation reproduced was the following:

$$\frac{\partial \bar{h}}{\partial \tau} = -\frac{\partial^2 h}{\partial X^2} - \alpha \frac{\partial^2 h}{\partial Y^2} + \frac{1}{2}\left[\left(\frac{\partial h}{\partial X}\right)^2 + \beta\left(\frac{\partial h}{\partial Y}\right)^2\right] - \left(\frac{\partial^4 h}{\partial X^4} + 2\frac{\partial^4 h}{\partial X^2 Y^2} + \frac{\partial^4 h}{\partial Y^4}\right) \tag{5.1}$$

Rost and Krug studied this equation evolution when $\alpha = 1$ and $\beta = -1$. In this situation, the cancellation of the two nonlinearities can break down the stabilization mechanism. Figure 63 shows their result for a system of size 500×500 starting from a random initial condition. Several parallel ridges nucleate and grow from the random background, spreading over the system. Solving Equation 5.1 with our semi-implicit splitting scheme, we obtained the results shown by Figure 64 (L_1 rate of variation per time) and Figure 65.

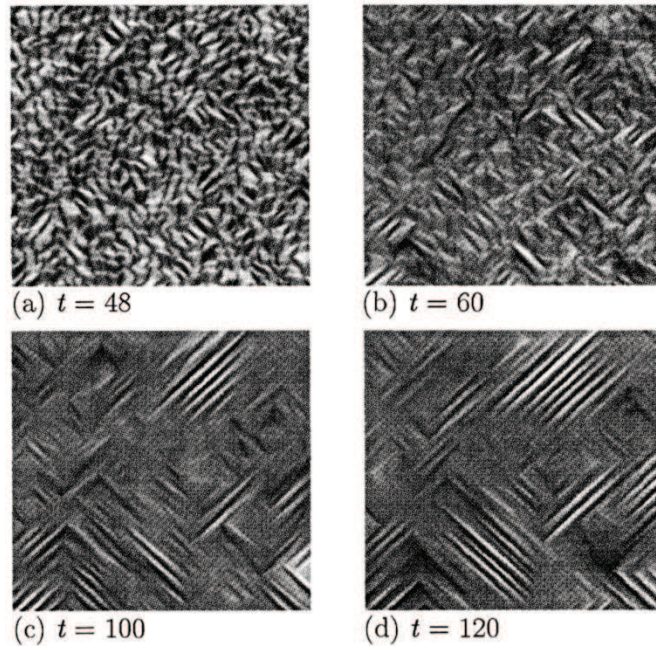(a) $t = 48$ (b) $t = 60$

(c) $t = 100$ (d) $t = 120$

Figure 63: Numerical result of Eq. 5.1 obtained by Rost and Krug (1995) [17]. The parameters were $\alpha = 1$ and $\beta = -1$ in order to cancel the nonlinearities. Parallel ridges nucleate and coalesce, taking over the system.
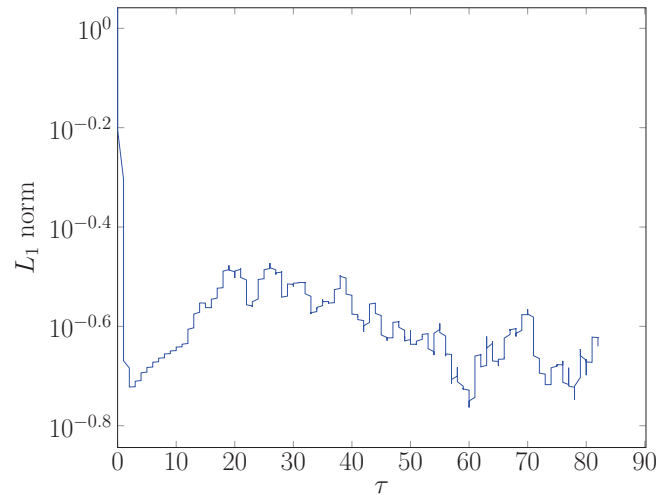
Figure 64: L_1 norm rate of variation per time for the reproduction of the results from Rost and Krug with the semi-implicit time splitting scheme.
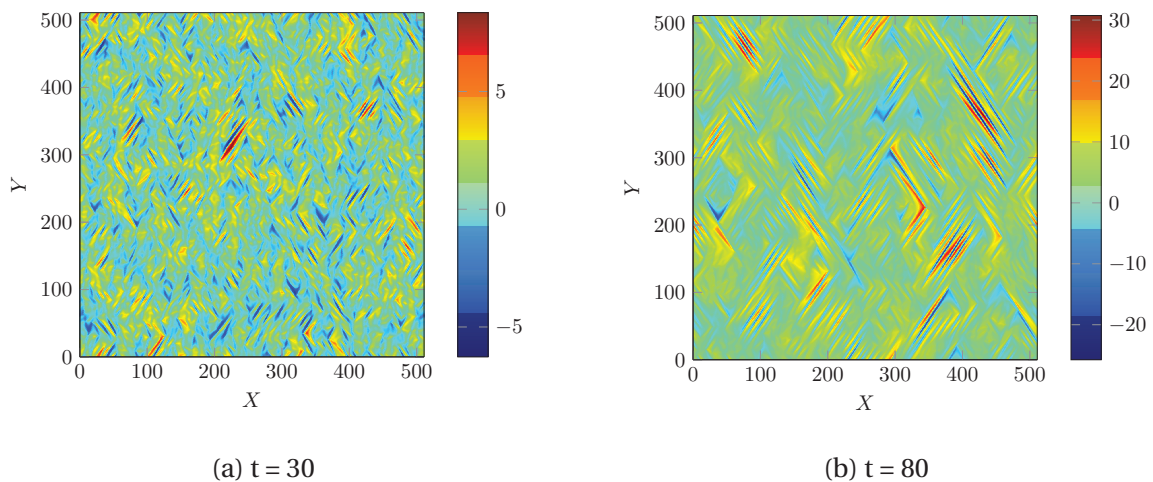

(a) t = 30

(b) t = 80

Figure 65: System of size 512 × 512, showing the evolution in time of Equation 5.1 with $\Delta\tau = 0.01$, $\alpha = 1$ and $\beta = -1$. The numerical results obtained through the semi-implicit time splitting reveals the nucleation and growth of parallel ridges.

As expected, the coalescence of parallel ridges were also present in our results, providing here another proof of reliability for the implemented scheme. We now proceed to the simulation of Equation 2.3 with $\theta = 66.17°$, with the parameters informed by Table 5. The damping coefficient was chosen as $\alpha = 0.1$ because of undesirable effects brought to the dynamics for this range of θ by higher values of α (heavy damping may lead to the disappearance of the structure with continuous decay of the mean height modulus).

Figure 66 and Figure 67 display the result from the $\theta = 66.17°$ simulation. In fact, the nonlinearities compensate each other when the system choses the $\vec{1}_x$ direction for the unstable modes. The nanostructure obtained for $\tau = 180$ is still irregular in terms of the ripple

Table 5: Parameters for the 66.17° simulation

Parameter	Values	Description
L	256	domain side
$\bar{\alpha}$	0.10	damping coefficient
$\bar{K}$	5	surface diffusion effects
$\Delta X, \Delta Y$	1	space step
θ	66.17°	angle of incidence of the beam
$\Delta \tau$	0.001	time step
a_μ	4	penetration depth/width of energy distribution

behavior, but the direction of preference is clear. There are approximately 23 wavelengths in the domain, which is less than the critical number of wavelengths from the linear stability analysis. In this case, we did not obtain a stationary structure, since the irregular ripple behavior keeps moving, although the pattern's preferred direction remains the same. This is sensed by the L_1 rate of change in time, as it stabilizes around $1 \times 10^{-1.8}$, when the structure reaches a configuration similar to $\tau = 180$ without ceasing the ripples' movement.
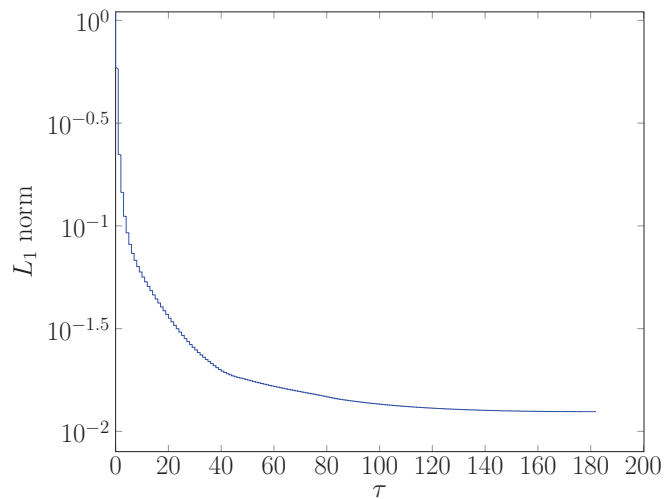

Figure 66: L_1 norm rate of change per time for $\theta = 66.17°$. Movements in the structure remain until the end, without reaching a stationary state.
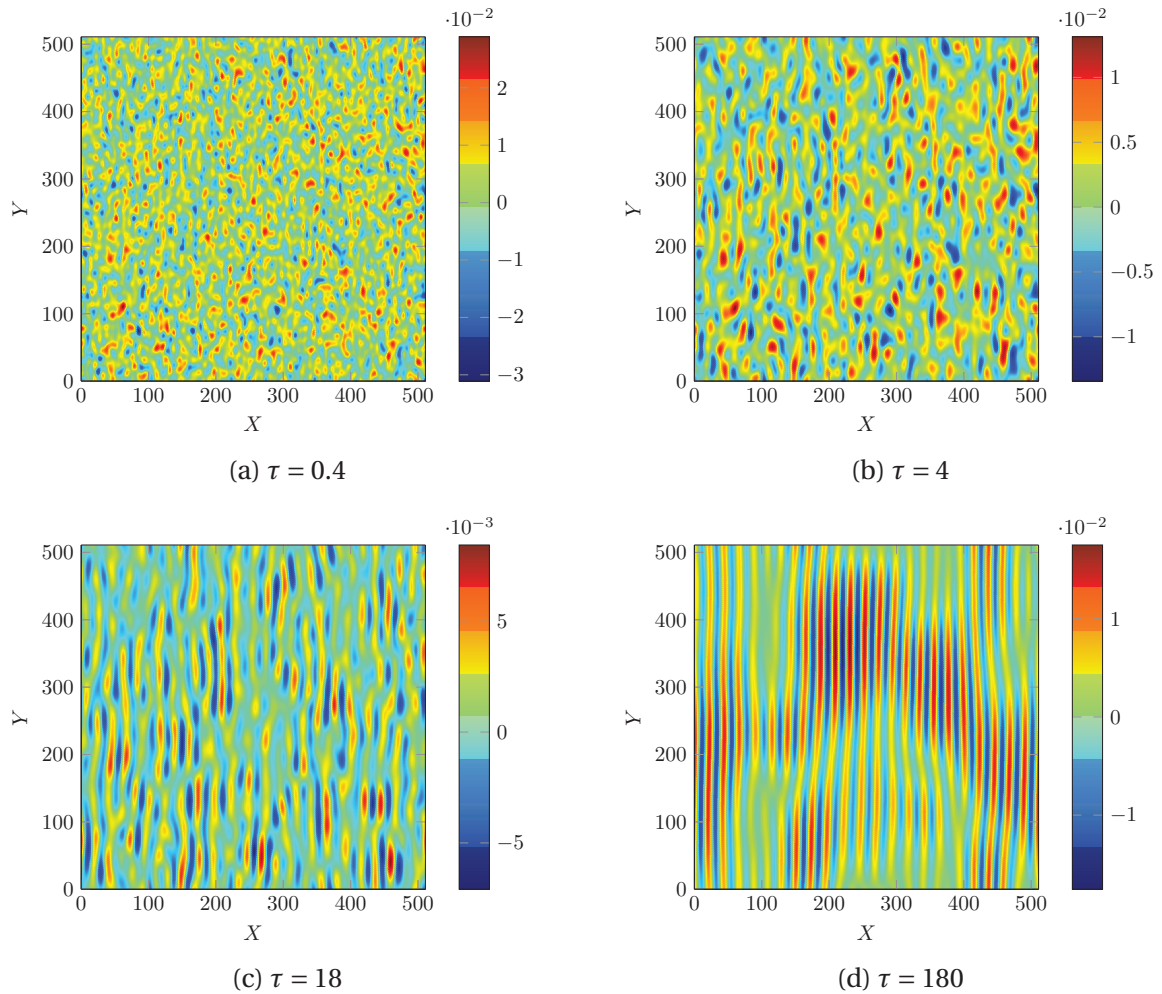
(a) $\tau = 0.4$

(b) $\tau = 4$

(c) $\tau = 18$

(d) $\tau = 180$

Figure 67: Simulation results for a system 512×512 with an angle $\theta = 66.17°$. The nonlinearities cancel each other and a well defined direction arises from the unstable mode. This is made clear by the selection of the $\vec{1}_x$ direction for $\tau = 180$.

Next, the anisotropy investigation due to angle variations moves toward higher values for the relative anisotropy. Here we conducted simulations for $\theta = 40°$, aiming to find the possible differences that could be introduced in the structure by the anisotropy, in relation to the previous studied $\theta = 30°$ cases. Therefore, the employed parameters were the same as those used throughout Chapter 3, except for the angle of incidence. The initial condition for the following case was a monomodal pattern with $\vec{q} = q_0 \vec{1}_Y$ ($q_0 = 2.5771 \cdot 10^{-2}$), which presented the same final morphology as the one obtained from a random initial profile.

Figure 68 suggests that the stationary state is reached as the L_1 rate of change decreases in the late time until the stop criterion is reached ($L_1 = 1 \cdot 10^{-7}$). The hexagonal modes emerge around $\tau = 500$, and they start to reorganize in structure, as seen in Figure 69 (a). A defectless pattern is obtained from this nonequilibrium dynamics, clearly shown by Figure 69 (b). A clean

spectrum of the most relevant modes (central part) acquired by the Fast Fourier Transform is displayed by Figure 69 (d). However, the final pattern is different from the $\theta = 30°$ case: here, the anisotropy effects lead to a diagonal connection between the cellular structure, resembling diagonal chains. This morphology is evident in the zoomed image from Figure 69 (c).
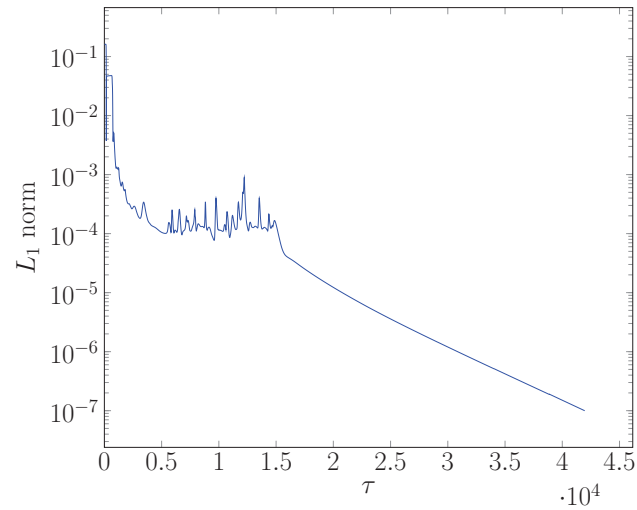

Figure 68: L_1 norm rate of change per time for $\theta = 40°$. Hexagonal modes emerge around $\tau = 500$ and the stationary state criteria is met at $\tau = 41,960$.
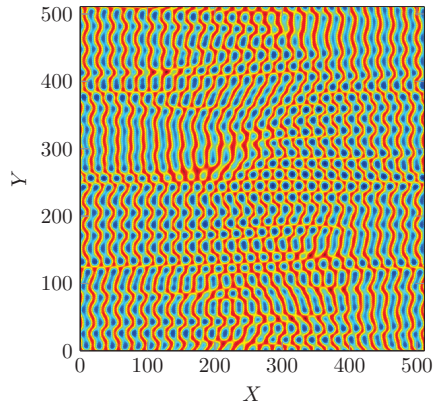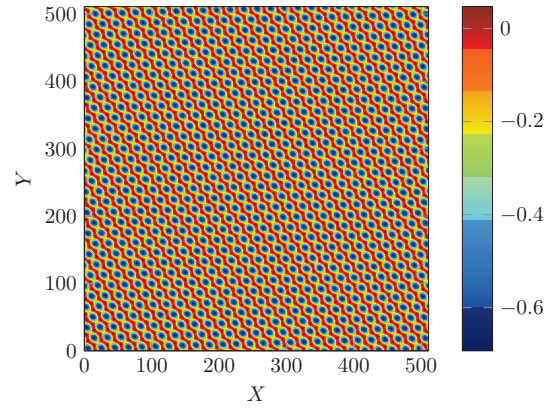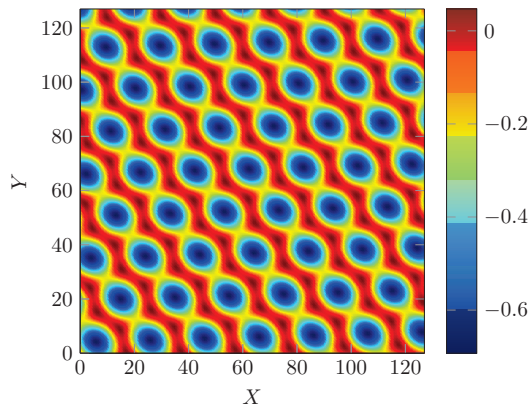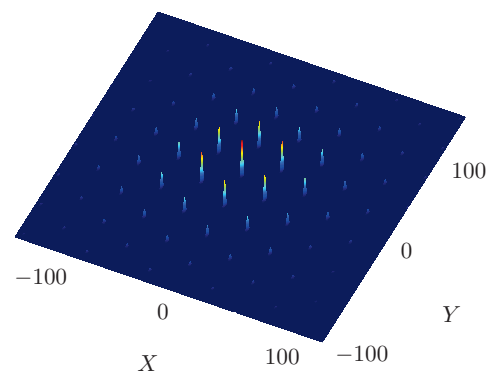
(a) $\tau = 750$

(b) $\tau = 41,960$

(c) $\tau = 41,960$ (zoom)

(d) $\tau = 41,960$ (FFT)

Figure 69: Simulation results for a system 512×512 with an angle $\theta = 40°$. Hexagonal modes emerge and reorganize the structure. The final pattern displays the cells connected in the diagonal, like chains.